

Searches for Light Dark Matter and Evidence of Coherent Elastic Neutrino-Nucleus Scattering of Solar Neutrinos with the LUX-ZEPLIN (LZ) Experiment

D.S. Akerib,^{1, 2} A.K. Al Musalhi,³ F. Alder,³ B.J. Almquist,⁴ C.S. Amarasinghe,⁵ A. Ames,^{1, 2} T.J. Anderson,^{1, 2} N. Angelides,⁶ H.M. Araújo,^{7, 8} J.E. Armstrong,⁹ M. Arthurs,^{1, 2} A. Baker,¹⁰ S. Balashov,⁸ J. Bang,⁴ J.W. Bargemann,⁵ E.E. Barillier,⁶ D. Bauer,⁷ K. Beattie,¹¹ A. Bhatti,⁹ T.P. Biesiadzinski,^{1, 2} H.J. Birch,⁶ E. Bishop,¹² G.M. Blockinger,¹³ C.A.J. Brew,⁸ P. Brás,¹⁴ S. Burdin,¹⁵ M.C. Carmona-Benitez,¹⁶ M. Carter,¹⁵ A. Chawla,¹⁷ H. Chen,¹¹ Y.T. Chin,¹⁶ N.I. Chott,¹⁸ S. Contreras,¹⁹ M.V. Converse,²⁰ R. Coronel,^{1, 2} A. Cottle,^{3, *} G. Cox,²¹ D. Curran,²¹ C.E. Dahl,^{22, 23} I. Darlington,³ S. Dave,³ A. David,³ J. Delgaudio,²¹ S. Dey,²⁴ L. de Viveiros,¹⁶ L. Di Felice,⁷ C. Ding,⁴ J.E.Y. Dobson,¹⁰ E. Druszkiewicz,²⁰ S. Dubey,⁴ C.L. Dunbar,²¹ S.R. Eriksen,²⁵ S. Fayer,⁷ N.M. Fearon,²⁴ N. Fieldhouse,²⁴ S. Fiorucci,¹¹ H. Flaecher,²⁵ E.D. Fraser,¹⁵ T.M.A. Fruth,²⁶ P.W. Gaemers,^{1, 2} R.J. Gaitskell,⁴ A. Geffre,²¹ J. Genovesi,^{16, 18} C. Ghag,³ J. Ghamsari,¹⁰ A. Ghosh,¹³ S. Ghosh,^{1, 2} R. Gibbons,^{11, 27} S. Gokhale,²⁸ J. Green,³ M.G.D. van der Grinten,⁸ J.J. Haiston,¹⁸ C.R. Hall,⁹ T. Hall,¹⁵ R.N. Hampf,⁶ S.J. Haselschwardt,²⁹ M.A. Hernandez,⁶ S.A. Hertel,³⁰ G.J. Homenides,³¹ M. Horn,²¹ D.Q. Huang,¹⁹ D. Hunt,^{24, 32} E. Jacquet,⁷ R. James,^{3, 33} K. Jenkins,¹⁴ A.C. Kaboth,¹⁷ A.C. Kamaha,¹⁹ M.K. Kannichankandy,¹³ D. Khaitan,²⁰ A. Khazov,⁸ J. Kim,⁵ Y.D. Kim,³⁴ D. Kodroff,^{11, †} E.V. Korolkova,³⁵ H. Kraus,²⁴ S. Kravitz,³² L. Kreczko,²⁵ V.A. Kudryavtsev,³⁵ C. Lawes,¹⁰ D.S. Leonard,³⁴ K.T. Lesko,¹¹ C. Levy,¹³ J. Lin,^{11, 27} A. Lindote,¹⁴ W.H. Lippincott,⁵ J. Long,²² M.I. Lopes,¹⁴ W. Lorenzon,²⁹ C. Lu,⁴ S. Luitz,^{1, 2} W. Ma,²⁴ V. Mahajan,²⁵ P.A. Majewski,⁸ A. Manalaysay,¹¹ R.L. Mannino,³⁶ R.J. Matheson,¹⁷ C. Maupin,²¹ M.E. McCarthy,²⁰ D.N. McKinsey,^{11, 27} J. McLaughlin,²² J.B. McLaughlin,³ R. McMonigle,¹³ B. Mitra,²² E. Mizrachi,^{1, 2, 9, 36} M.E. Monzani,^{1, 2, 37} K. Mora,⁶ E. Morrison,¹⁸ B.J. Mount,³⁸ M. Murdy,³⁰ A. St.J. Murphy,¹² H.N. Nelson,⁵ F. Neves,¹⁴ A. Nguyen,¹² C.L. O'Brien,³² F.H. O'Shea,^{1, 2} I. Olcina,^{11, 27} K.C. Oliver-Mallory,⁷ J. Orpwood,³⁵ K.Y. Oyulmaz,¹² K.J. Palladino,²⁴ N.J. Pannifer,²⁵ N. Parveen,¹³ S.J. Patton,¹¹ B. Penning,⁶ G. Pereira,¹⁴ E. Perry,¹¹ T. Pershing,³⁶ A. Piepke,³¹ S.S. Poudel,¹⁸ Y. Qie,²⁰ J. Reichenbacher,¹⁸ C.A. Rhyne,⁴ G.R.C. Rischbieter,^{6, 29} E. Ritchev,⁹ H.S. Riyat,^{12, 38} R. Rosero,²⁸ N.J. Rowe,²⁴ T. Rushton,³⁵ D. Rynders,²¹ S. Saltão,¹⁴ D. Santone,²⁴ I. Sargeant,⁸ A.B.M.R. Sazzad,^{31, 36} R.W. Schnee,¹⁸ G. Sehr,³² B. Shafer,⁹ S. Shaw,¹² W. Sherman,^{1, 2} K. Shi,²⁹ T. Shutt,^{1, 2} C. Silva,¹⁴ G. Sinev,¹⁸ J. Siniscalco,³ A.M. Slivar,³¹ R. Smith,^{11, 27} V.N. Solovov,¹⁴ P. Sorensen,¹¹ J. Soria,^{11, 27} T.J. Sumner,⁷ A. Swain,²⁴ M. Szydagis,¹³ D.R. Tiedt,²¹ M. Timalsina,¹¹ D.R. Tovey,³⁵ J. Tranter,³⁵ M. Trask,⁵ K. Trengove,¹³ M. Tripathi,³⁹ A. Usón,¹² A.C. Vaitkus,⁴ O. Valentino,⁷ V. Velan,¹¹ A. Wang,^{1, 2, †} J.J. Wang,³¹ Y. Wang,^{11, 27} L. Weeldreyer,⁵ T.J. Whitis,⁵ K. Wild,¹⁶ M. Williams,¹¹ J. Winnicki,^{1, 2} L. Wolf,¹⁷ F.L.H. Wolfs,²⁰ S. Woodford,^{12, 15} D. Woodward,¹¹ C.J. Wright,²⁵ Q. Xia,¹¹ J. Xu,³⁶ Y. Xu,¹⁹ M. Yeh,²⁸ D. Yeum,⁹ J. Young,¹⁰ W. Zha,¹⁶ H. Zhang,¹² T. Zhang,¹¹ and Y. Zhou⁷

(The LZ Collaboration)

¹SLAC National Accelerator Laboratory, Menlo Park, CA 94025-7015, USA

²Kavli Institute for Particle Astrophysics and Cosmology,
Stanford University, Stanford, CA 94305-4085 USA

³University College London (UCL), Department of Physics and Astronomy, London WC1E 6BT, UK

⁴Brown University, Department of Physics, Providence, RI 02912-9037, USA

⁵University of California, Santa Barbara, Department of Physics, Santa Barbara, CA 93106-9530, USA

⁶University of Zurich, Department of Physics, 8057 Zurich, Switzerland

⁷Imperial College London, Physics Department, Blackett Laboratory, London SW7 2AZ, UK

⁸STFC Rutherford Appleton Laboratory (RAL), Didcot, OX11 0QX, UK

⁹University of Maryland, Department of Physics, College Park, MD 20742-4111, USA

¹⁰King's College London, King's College London,
Department of Physics, London WC2R 2LS, UK

¹¹Lawrence Berkeley National Laboratory (LBNL), Berkeley, CA 94720-8099, USA

¹²University of Edinburgh, SUPA, School of Physics and Astronomy, Edinburgh EH9 3FD, UK

¹³University at Albany (SUNY), Department of Physics, Albany, NY 12222-0100, USA

¹⁴Laboratório de Instrumentação e Física Experimental de Partículas (LIP),
University of Coimbra, P-3004 516 Coimbra, Portugal

¹⁵University of Liverpool, Department of Physics, Liverpool L69 7ZE, UK

¹⁶Pennsylvania State University, Department of Physics, University Park, PA 16802-6300, USA

¹⁷Royal Holloway, University of London, Department of Physics, Egham, TW20 0EX, UK

¹⁸South Dakota School of Mines and Technology, Rapid City, SD 57701-3901, USA

¹⁹University of California, Los Angeles, Department of Physics & Astronomy, Los Angeles, CA 90095-1547

²⁰University of Rochester, Department of Physics and Astronomy, Rochester, NY 14627-0171, USA

²¹*South Dakota Science and Technology Authority (SDSTA), Sanford Underground Research Facility, Lead, SD 57754-1700, USA*

²²*Northwestern University, Department of Physics & Astronomy, Evanston, IL 60208-3112, USA*

²³*Fermi National Accelerator Laboratory (FNAL), Batavia, IL 60510-5011, USA*

²⁴*University of Oxford, Department of Physics, Oxford OX1 3RH, UK*

²⁵*University of Bristol, H.H. Wills Physics Laboratory, Bristol, BS8 1TL, UK*

²⁶*The University of Sydney, School of Physics, Physics Road, Camperdown, Sydney, NSW 2006, Australia*

²⁷*University of California, Berkeley, Department of Physics, Berkeley, CA 94720-7300, USA*

²⁸*Brookhaven National Laboratory (BNL), Upton, NY 11973-5000, USA*

²⁹*University of Michigan, Randall Laboratory of Physics, Ann Arbor, MI 48109-1040, USA*

³⁰*University of Massachusetts, Department of Physics, Amherst, MA 01003-9337, USA*

³¹*University of Alabama, Department of Physics & Astronomy, Tuscaloosa, AL 34587-0324, USA*

³²*University of Texas at Austin, Department of Physics, Austin, TX 78712-1192, USA*

³³*The University of Melbourne, School of Physics, Melbourne, VIC 3010, Australia*

³⁴*IBS Center for Underground Physics (CUP), Yuseong-gu, Daejeon, Korea*

³⁵*University of Sheffield, School of Mathematical and Physical Sciences, Sheffield S3 7RH, UK*

³⁶*Lawrence Livermore National Laboratory (LLNL), Livermore, CA 94550-9698, USA*

³⁷*Vatican Observatory, Castel Gandolfo, V-00120, Vatican City State*

³⁸*Black Hills State University, School of Natural Sciences, Spearfish, SD 57799-0002, USA*

³⁹*University of California, Davis, Department of Physics, Davis, CA 95616-5270, USA*

We present searches for light dark matter (DM) with masses 3–9 GeV/c^2 in the presence of coherent elastic neutrino-nucleus scattering ($\text{CE}\nu\text{NS}$) from ^8B solar neutrinos with the LUX-ZEPLIN experiment. This analysis uses a 5.7 tonne-year exposure with data collected between March 2023 and April 2025. In an energy range spanning 1–6 keV, we report no significant excess of events attributable to dark matter nuclear recoils, but we observe a significant signal from ^8B $\text{CE}\nu\text{NS}$ interactions that is consistent with expectation. We set world-leading limits on spin-independent and spin-dependent-neutron DM-nucleon interactions for masses down to 5 GeV/c^2 . In the no-dark-matter scenario, we observe a signal consistent with ^8B $\text{CE}\nu\text{NS}$ events, corresponding to a 4.5σ statistical significance. This is the most significant evidence of ^8B $\text{CE}\nu\text{NS}$ interactions and is enabled by robust background modeling and mitigation techniques. This demonstrates LZ’s ability to detect rare signals at keV-scale energies.

Introduction—Weakly interacting massive particles (WIMPs) remain a highly motivated dark matter (DM) candidate in the GeV/c^2 – TeV/c^2 mass range [1, 2]. The LUX-ZEPLIN (LZ) experiment currently sets the strongest constraints on DM-nucleon scattering cross-sections for masses greater than 9 GeV/c^2 [3]. Light DM candidates with masses less than 9 GeV/c^2 are well-motivated [4, 5], but present significant analysis challenges as they produce lower energy recoils. Additionally, at the increasingly smaller cross-sections probed by current generation xenon DM experiments, the sensitivity to light DM is limited by solar neutrinos undergoing coherent elastic neutrino-nucleus scattering ($\text{CE}\nu\text{NS}$) which form an irreducible ‘neutrino-fog’ background [1, 6–8]. Neutrinos from ^8B decays in the Sun [9] produce $\text{CE}\nu\text{NS}$ interactions, resulting in a nuclear recoil spectrum in xenon that closely resembles that of a 5.5 GeV/c^2 DM candidate. Previous results from the PandaX-4T and XENONnT experiments have revealed indications of solar ^8B $\text{CE}\nu\text{NS}$ interactions at significances lower than 3σ [10, 11], and have set limits on light DM nucleon cross-sections in this regime [12, 13]. In this Letter we present the first nuclear recoil DM search from LZ for DM of masses 3–9 GeV/c^2 and the first evidence of solar neutrino $\text{CE}\nu\text{NS}$ interactions on xenon, using a 5.7 tonne-year exposure.

Experiment—The LZ experiment [14, 15] operates underground in the Sanford Underground Research Facility (SURF) in Lead, South Dakota, USA, with a 4300 meter water-equivalent overburden to shield from cosmic radiation. At the center of the experiment is a dual-phase time projection chamber (TPC) containing seven tonnes of active liquid xenon. The TPC is surrounded by two subsystems, the liquid xenon Skin and the Outer Detector (OD), which serve as active vetoes to reject γ -ray and neutron backgrounds. The entire apparatus is immersed in 230 tonnes of ultrapure water, which passively shields from radioactivity in the underground cavern.

Particle interactions in the liquid xenon target typically produce either electron recoils (ERs) or nuclear recoils (NRs), generating prompt vacuum ultraviolet scintillation (S1) and ionization. Ionization electrons drift upward under the influence of an electric field. They are extracted into a thin layer of gaseous xenon above the liquid surface where they produce a delayed electroluminescence signal (S2). The S1 and S2 photons are observed by photomultiplier tube arrays above and below the active liquid xenon volume. The time interval between the S1 and the S2 pulses measures the drift time of the ionization, which is proportional to the interaction depth (z), while the transverse position (x, y) is reconstructed from the hit pattern of the S2 light in the top PMT array.

Dataset—The dataset for this analysis (WS2025) includes 546 live days collected between March 2023 and April 2025, extending the WS2024 dataset used in our previous dark matter search [3]. The TPC drift field was established at 97 V/cm and the extraction field in the liquid phase was 3.4 kV/cm. Dedicated americium-beryllium (AmBe) and deuterium-deuterium (DD) neutron calibrations were also performed during this additional calendar year.

We collect data using the data acquisition system described in [16], with a trigger efficiency of $95 \pm 1\%$ for S2 sizes corresponding to 4 extracted electrons. An event reconstruction algorithm identifies single scatter (SS) events with one prominent S1 and S2, with the efficiency shown in Figure 1. The loss in efficiency at low energy is driven by requiring that the S1 is observed in at least three PMTs. We quantify these inefficiencies with waveform simulations and calibration datasets: beta decays from an injected tritiated methane (CH_3T) source and AmBe neutron calibrations. Pulse shape variations from photon arrival times and electron drift diffusion result in additional losses, and are accounted for in the detector response modeling.

The calibration program of the TPC [17] allows for monitoring of detector spatial and temporal uniformity.

The (x, y, z) position- and time-dependent responses of the S1 and S2 signals are corrected using ^{222}Rn and ^{218}Po α -decay events present throughout the detector as in [3], allowing the definition of corrected quantities S1c and S2c in units of photons detected (phd). The scintillation and ionization gains for quanta produced in the liquid xenon are $g_1 = 0.112 \pm 0.002$ phd/photon and $g_2 = 34.0 \pm 0.9$ phd/electron [3].

The region-of-interest (ROI) is restricted to SS events where the S1 is observed in at least three PMTs with the S1c size that lies between 2 and 15 phd. The search parameter space spans an S2 range of 3.5–14.5 electrons (44.5 phd per extracted electron), disjointed from the ROI of [3]. The ROI approximately corresponds to nuclear recoil energies from 1–6 keV.

Selections—This ROI is contaminated by events from delayed charge and light emission after large energy depositions. After such events, we reject all data for a period of time that scales with the size of the energy deposition, resulting in a 16% loss of exposure, the dominant source of live time loss in the analysis. After removing periods of unstable detector conditions and elevated photon or electron rates, 417 live days remain.

A fiducial volume (FV) is defined to reject particle interactions occurring in proximity to the stainless steel high voltage grids and TPC wall. S2s in this analysis suffer from worsened (x, y) position resolution [18], compared to the larger S2s used in [3]. This motivates a stricter radial FV boundary, on average 5.4 cm from the wall and 15 cm from the PTFE-embedded high voltage resistors. We require < 0.01 total events originating

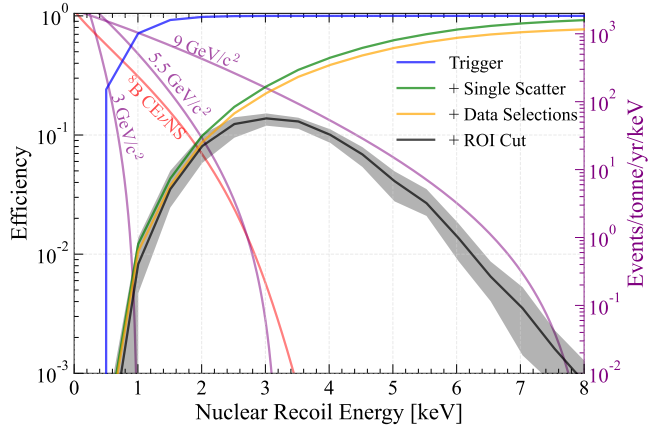


FIG. 1. Detection efficiency as a function of NR energy, after applying the S2 trigger (blue), ≥ 3 -fold SS reconstruction (green), analysis selections (orange), and region-of-interest (black) in sequence. The uncertainty band (gray) includes the uncertainties associated with the yields and fluctuations in the NR response model and the efficiency of single-scatter reconstruction and analysis selections. Also shown are the DM recoil spectra (purple) for masses of $3 \text{ GeV}/c^2$, $5.5 \text{ GeV}/c^2$, and $9 \text{ GeV}/c^2$, assuming a cross-section of 10^{-44} cm^2 , before the application of detection efficiency. The predicted ^8B CEvNS recoil spectrum (red) is similar to that of a DM particle with mass $5.5 \text{ GeV}/c^2$.

from the wall which sets the definition of the radial FV boundaries as a function of depth and azimuth. The vertical limits are unchanged from [3]. This results in a FV mass of 5.09 ± 0.15 tonnes compared to 5.5 ± 0.2 in [3], which is determined using tritium events. Events with S2s consistent with localized grid emission [19] are also removed through time and S2 (x, y) position-based selections using a computer vision algorithm [20], resulting in an additional 1% loss of exposure. The remaining 5.7 ± 0.2 tonne-years of exposure is used in this analysis.

Veto coincidence requirements reject external backgrounds such as radiogenic neutrons from spontaneous fission or (α, n) reactions [3]. Prompt coincidences of TPC events with pulses in the OD (≤ 300 ns) or Skin (≤ 250 ns) reject neutron scatters. Delayed coincidences (using a $\leq 600 \mu\text{s}$ time window following the main S1) target neutrons which thermalize, capture in the gadolinium-loaded liquid scintillator, and produce cascades of γ -rays following nuclear de-excitation. AmBe data taken during this period allowed for measuring a delayed neutron tagging efficiency in good agreement with measurements from americium-lithium (AmLi) data in [3]. Corresponding neutron simulations, corrected using AmBe and AmLi calibration data, predict the delayed (delayed + prompt) tagging efficiency of radiogenic neutrons to be $87 \pm 2\%$ ($92 \pm 4\%$) [3].

Finally, a series of selection criteria remove events inconsistent with xenon recoil signals in the fiducial volume. These criteria exploit the expected S1 and S2 spa-

tial pattern and pulse shapes of genuine events. Each selection was initially defined to maintain high acceptance of signals from calibration data. Selections with simple functional forms were then refined utilizing a covariance matrix adaptation evolution strategy (CMA-ES) [21] which simultaneously optimizes the signal-to-background ratio across multiple dimensions and outputs selections defined in the observables provided to the algorithm. The efficiency loss from these selections is shown in Figure 1.

Bias Mitigation—To reduce analyzer bias, we fabricate and insert artificial signal-like events into the raw dataset [22] by combining real S1 and S2 pulses from sequestered CH₃T and AmLi calibration data, respectively. We create two types of events: high mass DM-like scatters, following an exponential plus flat energy spectrum, described in [3]; and, for the latter 59% of this dataset, ⁸B CE ν NS-like scatters. The former type is designed for the ≥ 9 GeV/c² DM search and has a small expected contribution in this ROI, while the expected distribution from the latter provides good coverage. The expected number of artificial events after all selection criteria had a 90% probability of being between 0 and 3. The true number and type of artificial events inserted into the dataset was hidden from data analyzers until after the analysis was finalized. Subsequently, a single artificial event passing the ROI and fiducial volume selection was revealed. This event also passed our data selection. See the Supplemental Materials for more information on bias mitigation.

Response Modeling—The detector response model used to predict the response of xenon nuclear recoils is based on NEST 2.4.5 beta [23, 24] and tuned using a dedicated DD neutron dataset. The LZ DD generator provides a well-characterized source of nearly-monoenergetic 2.45 MeV neutrons producing NRs from the smallest detectable signals to the endpoint recoil, 1–74 keV [25, 26].

We constrain the NEST model describing the charge and light yields (Q_y and L_y , respectively) and their fluctuations as a function of energy using a Markov Chain Monte Carlo-based fitting method implemented with the EMCEE package [27]. Neutron recoils out to the DD endpoint are included in this fit to constrain the NEST model parameters across a large energy range, including higher energies outside of the ROI of this analysis. The DD dataset has limited ability to constrain the low-energy-specific yield parameters ($\lesssim 2.5$ keV), motivating our choice to enforce NEST priors derived from other existing measurements [25, 26, 28] for these parameters.

We include two important modifications to the NEST model described in [24]. First, fluctuations in S1 and S2 sizes are allowed to vary via the Fano-like factors F_{ex} and F_i , which control the variances of excitons and ions, respectively. We model F_{ex} as a linear function of exciton number where the slope and intercept are allowed to float freely. We find that F_i can be modeled as a constant. Second, we introduce an additional parameter

to allow recombination fluctuations, or the fluctuations governing the trade-off between Q_y and L_y , to be either sub- or supra-binomial. Both modifications are needed to achieve a good fit across the DD energy spectrum. Further details of this fitting procedure, including best fit parameters and corresponding yields models, are discussed in the Supplemental Materials and an upcoming publication.

Backgrounds—Accidental coincidence events and neutrons are background components in the search for ⁸B CE ν NS interactions. Events caused by electrons and γ -ray backgrounds produce S2 signals above the ROI of this analysis and are thus negligible. For the dark matter search, ⁸B CE ν NS is considered a background and is discussed in the following section.

Accidental coincidence events are comprised of S1-S2 pairs where the pulses do not originate from a common energy deposition. Instrumental effects, such as PMT dark counts [29] and spurious electron emission from the high voltage electrodes [19], produce isolated S1 and S2 pulses which can pile up within an event window. These events are modeled using a data-driven technique in which isolated pulses are combined at the waveform level to form synthetic SS events. In this ROI, the spectra of isolated S1 and S2 pulses are sensitive to variations in electron and photon rates occurring on millisecond timescales. Thus we perform an environment-matched pairing procedure where we pair isolated S1 and S2 pulses according to the ambient electron and photon rates. The result is a high-fidelity description of real accidental events.

A pure population of accidental coincidences can be found by searching for events with unphysical drift times (UDT), where the apparent drift time exceeds that of events originating at the cathode ($\gtrsim 1$ ms). This population provides a data-driven constraint on the accidental coincidence rate and is used to determine the normalization for the accidental model. The model is extensively validated with several ancillary datasets which probe a range of environments: UDT events, events with elevated photon and electron rates, AmLi calibration data, and events that fail the S1 and S2 pulse-based selections. The resulting goodness-of-fit tests [30] comparing the data and model prediction in binned S1c, S2c, and {S1c, S2c} distributions in these ancillary datasets all pass at a significance level of 0.05. More details are discussed in the Supplemental Materials and an upcoming publication.

After all selection criteria, the predicted number of accidental coincidences is 6.6 ± 0.3 events in the ROI for the 5.7 tonne-year exposure. The uncertainty is driven by both the number of UDT events at the point of normalization and the number of unique S1 and S2 pulses used in the accidental model. Additional systematic uncertainties are deemed unnecessary based on the good data-model agreement observed across the ancillary datasets. These datasets validate the normalization procedure and

TABLE I. Expected and best-fit counts for each background and/or signal component in various fit scenarios to the 19 observed events, as well as the value of the Gaussian-constrained nuisance parameter σ_{eff} . The second column shows the predicted counts and σ_{eff} value, the latter of which is 0 ± 1 by construction. The next three columns show fits where the ${}^8\text{B}$ signal is incorporated as a background component following the expectation in the first column; results from a background-only fit, where the ${}^8\text{B}$ signal is constrained, and signal-plus-background fits assuming a spin-independent dark matter particle with mass $3 \text{ GeV}/c^2$ and $9 \text{ GeV}/c^2$ are shown. The last column shows the fit with the ${}^8\text{B}$ rate unconstrained in the no-dark-matter hypothesis. The spin-independent (SI) DM, neutron, and ${}^8\text{B}$ CE ν NS uncertainties include systematics associated with the NR response modeling, the detection uncertainties, and the flux uncertainty (${}^8\text{B}$ CE ν NS only). The fitted values of σ_{eff} represent the shifts in the fitted component rates with respect to their predicted values due to the combined NR response modeling and detection efficiency uncertainties, in units of standard deviations.

Components	Expectation	Background-Only	$3 \text{ GeV}/c^2$	$9 \text{ GeV}/c^2$	${}^8\text{B}$ CE ν NS
		Fit	Fit	Fit	
SI DM	-	-	$0.5^{+5.1}_{-0.5}$	$0.0^{+4.1}_{-0.0}$	-
${}^8\text{B}$ CE ν NS	$20.6^{+8.9}_{-6.8}$	$15.0^{+2.9}_{-2.5}$	$14.7^{+3.1}_{-2.7}$	$15.0^{+2.9}_{-2.5}$	$12.3^{+7.0}_{-5.4}$
Accidental coinc.	6.6 ± 0.3	6.5 ± 0.3	6.5 ± 0.3	6.5 ± 0.3	6.6 ± 0.3
Detector neutrons	$0.04^{+0.25}_{-0.04}$	$0.1^{+0.2}_{-0.1}$	$0.1^{+0.2}_{-0.1}$	$0.1^{+0.2}_{-0.1}$	$0.1^{+0.2}_{-0.1}$
Total	$27.2^{+10.1}_{-7.3}$	$21.6^{+4.7}_{-3.8}$	$21.7^{+7.1}_{-4.2}$	$21.6^{+6.2}_{-3.8}$	$18.9^{+7.0}_{-5.5}$
σ_{eff}	0 ± 1	$-0.81^{+0.59}_{-0.60}$	$-0.86^{+0.63}_{-0.69}$	$-0.81^{+0.58}_{-0.60}$	0 ± 1

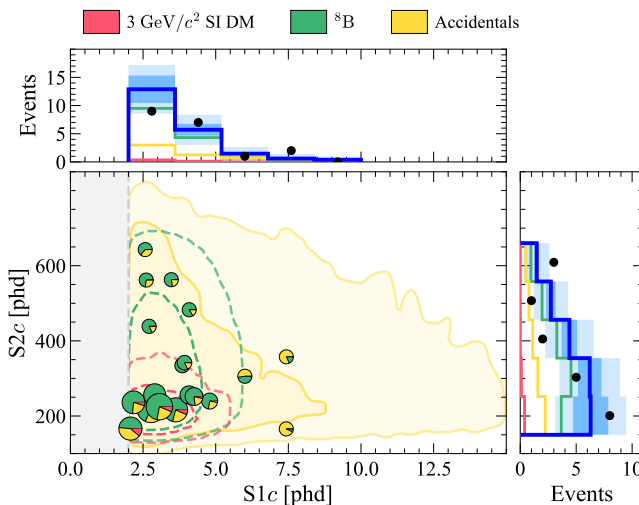


FIG. 2. The 19 events comprising the final dataset passing all selections are shown as individual pie charts in the observable space $\{S1c, S2c\}$. Each pie chart depicts the relative fit contributions from the accidental coincidences (yellow) and ${}^8\text{B}$ CE ν NS (green) background components along with a $3 \text{ GeV}/c^2$ DM candidate (pink). The relative size of each pie chart is proportional to its contribution to $3 \text{ GeV}/c^2$ DM events. Contours enclose 1σ and 2σ model distributions. The data (black points) and best-fit model (solid blue line) in $S1c$ and $S2c$ projections are also shown. Shaded light blue (dark blue) bands depict the total (systematic-only) model uncertainty. The detector neutron component is subdominant and therefore not shown.

confirm the ability to accurately model populations with varying underlying accidental coincidence sources.

Dark Matter Search—After the application of all data

selection criteria and the removal of the one artificial event, 19 events remain in the ROI (see Figure 2). The search for dark matter is conducted with a two-sided unbinned profile likelihood ratio test statistic defined in the observable space $\{S1c, S2c\}$ [31, 32].

The components of the likelihood describing particle interactions — detector neutrons, ${}^8\text{B}$ CE ν NS, and the dark matter signal — are constructed with the xenon response model described above and an event simulation framework [33]. We account for the systematic uncertainty on the light and charge yields, the quanta fluctuations, and the detector efficiency in the likelihood. This is incorporated through a single Gaussian constraint with nuisance parameter σ_{eff} controlling the combined rate uncertainty, the scale of which depends on the individual recoil spectra. The change in rate due to a $+1$ (-1) standard deviation shift in σ_{eff} varies as a function of DM mass, from $+103\%$ (-59%) at $3 \text{ GeV}/c^2$ to $+21\%$ (-20%) at $9 \text{ GeV}/c^2$.

We constrain the detector neutron rate *in situ* by including an additional dataset in the likelihood which requires events to pass all data selection criteria except the delayed coincidence veto. One event survives the selection. The best-fit number of neutron events in this sideband dataset is $0.3^{+1.7}_{-0.3}$, which is consistent with predictions from simulations. The neutron veto efficiency, incorporated as a Gaussian constraint, relates this sideband dataset to the main science dataset, while the other background components are related via the false veto probability from random coincidences (3%).

The expected number of events in the main science dataset from ${}^8\text{B}$ CE ν NS interactions, accidental coincidences, and detector neutrons is shown in Table I. The

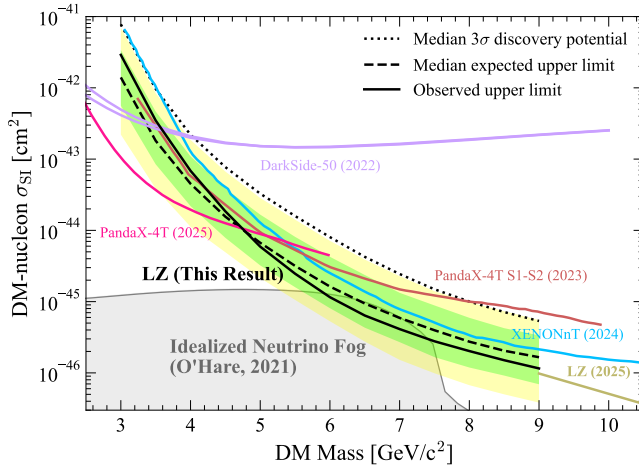


FIG. 3. Upper limits (90% C.L.) on the spin-independent DM-nucleon cross section as a function of DM mass using the 5.7 tonne-year dataset are shown in the solid black line. The range of expected upper limits from background-only experiments are shown as green and yellow regions for 68% and 95% of experiments, respectively. The dashed black line shows the median expected upper limit, while the dotted black line shows the median 3σ discovery potential, using the post-fit model. The onset of the neutrino fog, as defined in [8], is shown as the shaded gray region. Other experimental limits are also shown [12, 13, 34, 35].

uncertainties are incorporated in the likelihood as constraints on their respective rates. The accidental rate is Gaussian-constrained. The ${}^8\text{B}$ CE ν NS rate has an additional 4% flux uncertainty imposed as a Gaussian constraint [32].

The best-fit model and data in the $\{\text{S}1c, \text{S}2c\}$ analysis space and its projections are also shown in Figure 2. The background-only model is evaluated using binned goodness-of-fit tests, with p-values of 0.51, 0.44, and 0.53 in $\text{S}1c$, $\text{S}2c$, and $\{\text{S}1c, \text{S}2c\}$ spaces, respectively. All data-model comparisons show good agreement.

The 90% confidence level upper limit on the spin-independent DM-nucleon cross section as a function of mass is shown in Figure 3. The observed upper limit spans from $2.9 \times 10^{-42} \text{ cm}^2$ at $3 \text{ GeV}/c^2$ to $1.2 \times 10^{-46} \text{ cm}^2$ at $9 \text{ GeV}/c^2$. Results for the spin-dependent DM-nucleon coupling scenario are shown in the Appendix.

Boron-8 CE ν NS Measurement—We also perform a measurement of the ${}^8\text{B}$ CE ν NS process on xenon nuclei with the same dataset assuming zero dark matter events. Using the q_0 test statistic [31], we reject the hypothesis of zero ${}^8\text{B}$ CE ν NS events with a statistical significance of 4.5σ . The median expected significance is $6.7^{+2.4}_{-2.2}\sigma$. The best-fit value of ${}^8\text{B}$ CE ν NS counts of $12.3^{+7.0}_{-5.4}$ is shown in the last column of Table I and is consistent with the prediction of $20.6^{+8.9}_{-6.8}$.

The detection of the ${}^8\text{B}$ solar neutrino CE ν NS process enables measurements of various quantities of physical

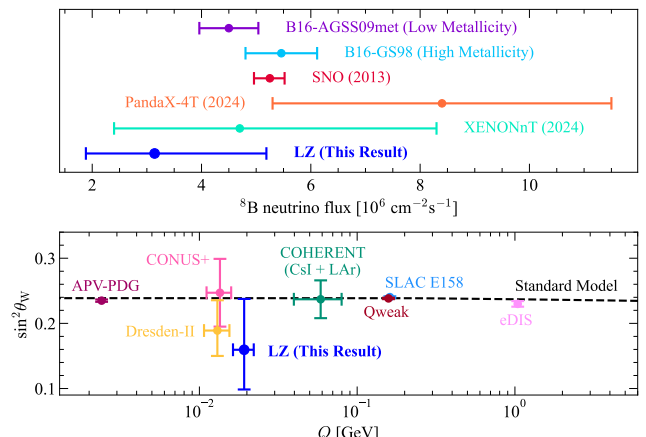


FIG. 4. *Top:* Measurement of ${}^8\text{B}$ solar neutrino flux assuming the SM-predicted CE ν NS cross-section and weak mixing angle. Predictions from low- and high-metallicity solar models are shown [36] alongside other experimental measurements [10, 11, 37]. *Bottom:* Measurement of the weak mixing angle assuming the SNO measurement of ${}^8\text{B}$ solar- ν flux and SM-predicted CE ν NS cross-section is shown. Also shown are other experimental results [38–44] and the SM prediction [45].

interest (Figure 4) within the Standard Model (SM). Assuming the SM-predicted CE ν NS cross-section and weak mixing angle, the ${}^8\text{B}$ solar neutrino flux is found to be $3.1^{+2.1}_{-1.3} \times 10^6 \text{ cm}^{-2}\text{s}^{-1}$, in good agreement with [36]. Adopting the SNO measured ${}^8\text{B}$ flux [37] and SM weak mixing angle, the flux-weighted CE ν NS cross-section on xenon is found to be $7.4^{+4.8}_{-3.0} \times 10^{-40} \text{ cm}^2$. The SM prediction is $1.2 \times 10^{-39} \text{ cm}^2$. Assuming the SNO measured ${}^8\text{B}$ flux and SM prediction for CE ν NS cross-section on xenon, the SM weak mixing angle at an average momentum transfer of $19.2 \pm 2.9 \text{ MeV}/c$ is found to be $\sin^2 \theta_W = 0.16^{+0.08}_{-0.06}$. We compute the momentum transfer as $Q = \sqrt{2m_{\text{Xe}}E_r}$, averaging over the natural isotopic abundances of xenon to calculate the xenon nuclear mass m_{Xe} , and using the mean ${}^8\text{B}$ CE ν NS nuclear recoil energy E_r predicted by our simulation including detection efficiencies ($1.5 \pm 0.5 \text{ keV}$). All of these measurements are consistent with SM expectations and previous measurements.

Conclusions—LZ has achieved limits on SI DM-nucleon interactions that are world-leading above $5 \text{ GeV}/c^2$. The sensitivity and robustness of this analysis is enabled by careful calibration of the detector nuclear recoil response, with a comprehensive treatment of light and charge yields as well as their fluctuations, and excellent mitigation and modeling of accidental coincidences down to S2s of 3.5 electrons that would otherwise impede DM searches with masses less than $9 \text{ GeV}/c^2$. We present the strongest evidence to date for CE ν NS on xenon from solar neutrinos at a significance of 4.5σ , which demonstrates LZ’s ability to detect nuclear recoil signals

of astrophysical origin. Using the detected ${}^8\text{B}$ $\text{CE}\nu\text{NS}$ interactions, we present measurements of the weak mixing angle and $\text{CE}\nu\text{NS}$ cross-section on xenon. The measured ${}^8\text{B}$ $\text{CE}\nu\text{NS}$ flux is found to be consistent with that measured by the SNO collaboration. The LZ experiment continues to take data towards a target 1000-day exposure that will allow for further dark matter searches into the neutrino fog and enable improved measurements of the $\text{CE}\nu\text{NS}$ process.

Acknowledgements — The research supporting this work took place in part at the Sanford Underground Research Facility (SURF) in Lead, South Dakota. Funding for this work is supported by the U.S. Department of Energy, Office of Science, Office of High Energy Physics under Contract Numbers DE-AC02-05CH11231, DE-SC0020216, DE-SC0012704, DE-SC0010010, DE-AC02-07CH11359, DE-SC0015910, DE-SC0014223, DE-SC0010813, DE-SC0009999, DE-NA0003180, DE-SC0011702, DE-SC0010072, DE-SC0006605, DE-SC0008475, DE-SC0019193, DE-FG02-10ER46709, UW PRJ82AJ, DE-SC0013542, DE-AC02-76SF00515, DE-SC0018982, DE-SC0019066, DE-SC0015535, DE-SC0019319, DE-SC0025629, DE-SC0024114, DE-AC52-07NA27344, & DE-SC0012447. This research was also supported by the UKRI's Science & Technology Facilities Council under award numbers ST/W000490/1, ST/W000482/1, ST/W000636/1, ST/W000466/1, ST/W000628/1, ST/W000555/1, ST/W000547/1, ST/W00058X/1, ST/X508263/1, ST/V506862/1, ST/X508561/1, ST/V507040/1, ST/W507787/1, ST/R003181/1, ST/R003181/2, ST/W507957/1, ST/X005984/1, ST/X006050/1; Portuguese Foundation for Science and Technology (FCT) under award numbers PTDC/FIS-PAR/2831/2020; the Institute for Basic Science, Korea (budget number IBS-R016-D1); the Swiss National Science Foundation (SNSF) under award number 10001549. This research was supported by the Australian Government through the Australian Research Council Centre of Excellence for Dark Matter Particle Physics under award number CE200100008. We acknowledge additional support from the UK Science & Technology Facilities Council (STFC) for PhD studentships and the STFC Boulby Underground Laboratory in the U.K., the GridPP [46, 47] and IRIS Collaborations, in particular at Imperial College London and additional support by the University College London (UCL) Cosmoparticle Initiative, and the University of Zurich. We acknowledge additional support from the Center for the Fundamental Physics of the Universe, Brown University. K.T. Lesko acknowledges the support of Brasenose College and Oxford University. This research used resources of the National Energy Research Scientific Computing Center, a DOE Office of Science User Facility supported by the Office of Science of the U.S. Department of Energy under Contract No. DE-AC02-05CH11231. We gratefully acknowledge support

from GitLab through its GitLab for Education Program. The University of Edinburgh is a charitable body, registered in Scotland, with the registration number SC005336. The assistance of SURF and its personnel in providing physical access and general logistical and technical support is acknowledged. We acknowledge the South Dakota Governor's office, the South Dakota Community Foundation, the South Dakota State University Foundation, and the University of South Dakota Foundation for use of xenon. We also acknowledge the University of Alabama for providing xenon. For the purpose of open access, the authors have applied a Creative Commons Attribution (CC BY) license to any Author Accepted Manuscript version arising from this submission. Finally, we respectfully acknowledge that we are on the traditional land of Indigenous American peoples and honor their rich cultural heritage and enduring contributions. Their deep connection to this land and their resilience and wisdom continue to inspire and enrich our community. We commit to learning from and supporting their effort as original stewards of this land and to preserve their cultures and rights for a more inclusive and sustainable future.

Appendix - Spin Dependent DM Results

The treatment of spin-dependent models follows the procedure in Refs. [3, 48]. Refs. [49–51] describe the neutron-only and proton-only nuclear structure functions, with the structure functions from [49] treated as the nominal model. These structure functions are used as inputs to model DM scattering on ${}^{129}\text{Xe}$ and ${}^{131}\text{Xe}$.

Upper limits (90% confidence-level) on the spin-dependent cross-section as a function of DM mass are shown in Figure 5 in both the DM-neutron and DM-proton coupling scenarios with the nuclear structure function uncertainty depicted as the gray band. The dotted black line depicts the 3σ discovery potential. The strongest limit is set for a DM mass of 9 GeV/c^2 at a cross section of $\sigma_{\text{SD}}^n = 1.8 \times 10^{-41} \text{ cm}^2$ in the DM-neutron scenario, and at 9 GeV/c^2 at a cross section of $\sigma_{\text{SD}}^p = 5.6 \times 10^{-40} \text{ cm}^2$ in the DM-proton scenario.

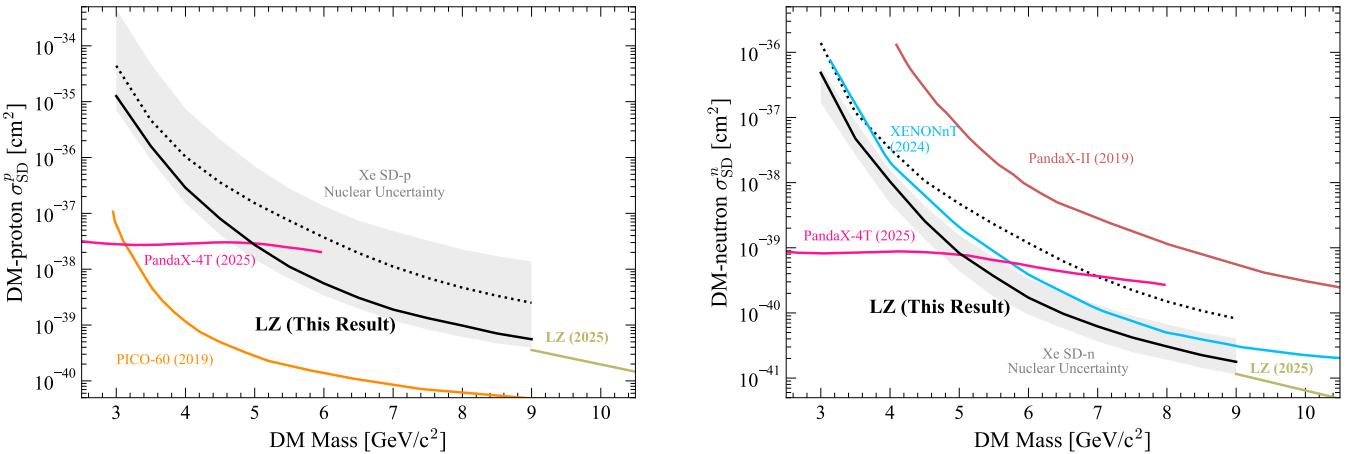


FIG. 5. Upper limits (90% C.L.) from the 5.7 tonne-year analysis on the spin-dependent DM-proton (left) and DM-neutron (right) cross-section as a function of DM mass are shown with a solid black line. The observed limit uses the mean of the nuclear structure functions from [49], with the gray band depicting the uncertainty from nuclear modeling in the models described in [49–51]. The median 3σ discovery potential using the post-fit model is shown as the dotted black line. Other experimental limits for spin-dependent DM-proton [3, 13, 52] and DM-neutron [3, 13, 53] scattering are also shown.

* a.cottle@ucl.ac.uk
 † danielkodroff@lbl.gov
 ‡ awang5@slac.stanford.edu

[1] D. S. Akerib *et al.*, *Snowmass 2021*, (2022), arXiv:2203.08084 [hep-ex].
 [2] J. Billard *et al.*, *Rept. Prog. Phys.* **85**, 056201 (2022), arXiv:2104.07634 [hep-ex].
 [3] J. Aalbers *et al.* (LZ Collaboration), *Phys. Rev. Lett.* **135**, 011802 (2025), arXiv:2410.17036 [hep-ex].
 [4] D. E. Kaplan, M. A. Luty, and K. M. Zurek, *Phys. Rev. D* **79**, 115016 (2009), arXiv:0901.4117 [hep-ph].
 [5] T. Cohen, D. J. Phalen, A. Pierce, and K. M. Zurek, *Phys. Rev. D* **82**, 056001 (2010), arXiv:1005.1655 [hep-ph].
 [6] J. Billard, L. Strigari, and E. Figueroa-Feliciano, *Phys. Rev. D* **89**, 023524 (2014), arXiv:1307.5458 [hep-ph].
 [7] F. Ruppin, J. Billard, E. Figueroa-Feliciano, and L. Strigari, *Phys. Rev. D* **90**, 083510 (2014), arXiv:1408.3581 [hep-ph].
 [8] C. A. J. O'Hare, *Phys. Rev. Lett.* **127**, 251802 (2021), arXiv:2109.03116 [hep-ph].
 [9] J. N. Bahcall, A. M. Serenelli, and S. Basu, *Astrophys. J. Lett.* **621**, L85 (2005), arXiv:astro-ph/0412440.
 [10] Z. Bo *et al.* (PandaX), *Phys. Rev. Lett.* **133**, 191001 (2024), arXiv:2407.10892 [hep-ex].
 [11] E. Aprile *et al.* (XENON), *Phys. Rev. Lett.* **133**, 191002 (2024), arXiv:2408.02877 [nucl-ex].
 [12] E. Aprile *et al.* (XENON), *Phys. Rev. Lett.* **134**, 111802 (2025), arXiv:2409.17868 [hep-ex].
 [13] M. Zhang *et al.* (PandaX), *Phys. Rev. Lett.* **135**, 211001 (2025), arXiv:2507.11930 [hep-ex].
 [14] B. J. Mount *et al.*, (2017), arXiv:1703.09144 [physics.ins-det].
 [15] D. S. Akerib *et al.* (LZ), *Nucl. Instrum. Meth. A* **953**, 163047 (2020), arXiv:1910.09124 [physics.ins-det].
 [16] J. Aalbers *et al.* (LZ Collaboration), *Nucl. Instrum.*

Methods Phys. Res. Sect. A **1068**, 169712 (2024), 2405.14732.
 [17] J. Aalbers *et al.* (LZ), *JINST* **19** (08), P08027, arXiv:2406.12874 [physics.ins-det].
 [18] J. Aalbers *et al.* (LZ), *Phys. Rev. D* **108**, 012010 (2023), arXiv:2211.17120 [hep-ex].
 [19] D. S. Akerib *et al.*, (2025), arXiv:2510.06500 [physics.ins-det].
 [20] G. Bradski, *Dr. Dobb's Journal of Software Tools* (2000).
 [21] N. Hansen, Y. Akimoto, and P. Baudis, *CMA-ES/pycma* on Github, Zenodo, DOI:10.5281/zenodo.2559634 (2019).
 [22] J. A. Klein and A. Roodman, *Annual Review of Nuclear and Particle Science* **55**, 141 (2005).
 [23] M. Szydagis *et al.*, *Noble Element Simulation Technique*, v2.4.5 beta (2025).
 [24] M. Szydagis *et al.*, *Front. Detect. Sci. Tech.* **2**, 1480975 (2024), arXiv:2211.10726 [hep-ex].
 [25] D. S. Akerib *et al.* (LUX), (2016), arXiv:1608.05381 [physics.ins-det].
 [26] D. S. Akerib *et al.* (LUX), *Phys. Rev. Lett.* **134**, 061002 (2025), arXiv:2210.05859 [physics.ins-det].
 [27] D. Foreman-Mackey, D. W. Hogg, D. Lang, and J. Goodman, *PASP* **125**, 306 (2013), arXiv:1202.3665 [astro-ph.IM].
 [28] B. Lenardo *et al.*, (2019), arXiv:1908.00518 [physics.ins-det].
 [29] D. S. Akerib *et al.*, (2021), arXiv:2101.08753 [astro-ph.IM].
 [30] S. Baker and R. D. Cousins, *Nuclear Instruments and Methods in Physics Research* **221**, 437 (1984).
 [31] G. Cowan, K. Cranmer, E. Gross, and O. Vitells, *Eur. Phys. J. C* **71**, 1554 (2011), [Erratum: *Eur.Phys.J.C* 73, 2501 (2013)], arXiv:1007.1727 [physics.data-an].
 [32] D. Baxter *et al.*, *Eur. Phys. J. C* **81**, 907 (2021), arXiv:2105.00599 [hep-ex].
 [33] D. S. Akerib *et al.* (LZ), *Astropart. Phys.* **125**, 102480 (2021), arXiv:2001.09363 [physics.ins-det].
 [34] W. Ma *et al.* (PandaX Collaboration), *Phys. Rev. Lett.*

130, 021802 (2023), arXiv:2207.04883 [hep-ex].

[35] P. Agnes *et al.* (DarkSide-50 Collaboration), Phys. Rev. D **107**, 063001 (2023), arXiv:2207.11966 [hep-ex].

[36] N. Vinyoles, A. M. Serenelli, F. L. Villante, S. Basu, J. Bergström, M. C. Gonzalez-Garcia, M. Maltoni, C. Peña-Garay, and N. Song, *Astrophys. J.* **835**, 202 (2017), arXiv:1611.09867 [astro-ph.SR].

[37] B. Aharmim *et al.* (SNO), Phys. Rev. C **88**, 025501 (2013), arXiv:1109.0763 [nucl-ex].

[38] C. S. Wood, S. C. Bennett, D. Cho, B. P. Masterson, J. L. Roberts, C. E. Tanner, and C. E. Wieman, *Science* **275**, 1759 (1997).

[39] P. L. Anthony *et al.* (SLAC E158), Phys. Rev. Lett. **95**, 081601 (2005), arXiv:hep-ex/0504049.

[40] D. Androić *et al.* (Qweak), *Nature* **557**, 207 (2018), arXiv:1905.08283 [nucl-ex].

[41] V. De Romeri, O. G. Miranda, D. K. Papoulias, G. Sanchez Garcia, M. Tórtola, and J. W. F. Valle, JHEP **04**, 035, arXiv:2211.11905 [hep-ph].

[42] D. Aristizabal Sierra, V. De Romeri, and D. K. Papoulias, JHEP **09**, 076, arXiv:2203.02414 [hep-ph].

[43] V. De Romeri, D. K. Papoulias, and G. Sanchez Garcia, Phys. Rev. D **111**, 075025 (2025), arXiv:2501.17843 [hep-ph].

[44] C. Prescott *et al.*, Physics Letters B **84**, 524 (1979).

[45] S. Navas *et al.* (Particle Data Group), Phys. Rev. D **110**, 030001 (2024).

[46] P. Faulkner *et al.*, J. Phys. G **32**, N1 (2006).

[47] D. Britton *et al.*, Philos. Trans. R. Soc. A **367**, 2447 (2009).

[48] J. Aalbers *et al.* (LZ Collaboration), Phys. Rev. Lett. **131**, 041002 (2023), arXiv:2207.03764 [hep-ex].

[49] M. Hoferichter, J. Menéndez, and A. Schwenk, Phys. Rev. D **102**, 074018 (2020), arXiv:2007.08529 [hep-ph].

[50] P. Pirinen, J. Kotila, and J. Suhonen, Nucl. Phys. A **992**, 121624 (2019).

[51] B. S. Hu, J. Padua-Argüelles, S. Leutheusser, T. Miyagi, S. R. Stroberg, and J. D. Holt, Phys. Rev. Lett. **128**, 072502 (2022), arXiv:2109.00193 [nucl-th].

[52] C. Amole *et al.* (PICO), Phys. Rev. D **100**, 022001 (2019), arXiv:1902.04031 [astro-ph.CO].

[53] E. Aprile *et al.* (XENON Collaboration), Phys. Rev. Lett. **131**, 041003 (2023), arXiv:2303.14729 [hep-ex].

[54] C. Rhyne, *Development of Tagged Low Energy D- and H-Based Scintillator Reflector Neutron Sources and Characterizations of a D-D Neutron Generator for Calibrations of the LZ Detector*, PhD Thesis, Brown University (2024).

[55] E. Mendoza, D. Cano-Ott, T. Koi, and C. Guerrero, IEEE Transactions on Nuclear Science **61**, 2357 (2014).

[56] M. Chadwick, M. Herman, P. Obložinský, *et al.*, Nuclear Data Sheets **112**, 2887 (2011), special Issue on ENDF/B-VII.1 Library.

[57] M. Szydagis *et al.*, Noble Element Simulation Technique, v2.4.0 (2023).

[58] J. Aalbers *et al.* (LZ Collaboration), (2025), arXiv:2509.16281 [physics.ins-det].

[59] E. Aprile *et al.* (XENON Collaboration), (2024), arXiv:2412.10451 [physics.ins-det].

[60] E. Aprile, M. Anthony, Q. Lin, Z. Greene, P. De Perio, F. Gao, J. Howlett, G. Plante, Y. Zhang, and T. Zhu, Phys. Rev. D **98**, 112003 (2018), arXiv:1809.02072 [physics.ins-det].

[61] T. Pershing *et al.*, Phys. Rev. D **106**, 052013 (2022), arXiv:2207.08326 [physics.ins-det].

[62] D. Huang, *Ultra-Low Energy Calibration of the LUX and LZ Dark Matter Detectors*, Ph.D. thesis, Brown U. (2020).

Supplemental Materials

Details of the Accidental Coincidence Model and Validation

We construct the accidental coincidence model with two major ingredients: a high statistics synthetic dataset generated from real data and a sideband of single scatter events with unphysically long drift times to constrain the overall rate. To produce the synthetic dataset, we draw S1 and S2 pulses from non-scatter events which pass a minimal set of data quality criteria and loose pulse selections. We then combine the pulses and their surrounding electron and photon environments together at the waveform level to form accidental coincidence events. This procedure produces synthetic events with both physical drift times ($\lesssim 1$ ms) and unphysical drift times ($\gtrsim 1$ ms).

We normalize the model by scaling the rate of synthetic unphysical drift time (UDT) events to a sideband dataset consisting of UDT events. This dataset spans a broad range of pulse areas, inclusive of the ROI, with S1s between 2 and 15 phd and S2s up to 10^4 phd. We impose a limited set of data selections to maintain sufficient statistics; namely, the S2 ROI, fiducial volume, and several S1 and S2 pulse-based selections are not applied.

After normalization, we apply the remaining data selection criteria to the synthetic physical drift time events to produce the final accidental coincidence prediction in $\{S1c, S2c\}$. We use the synthetic dataset to derive the predicted ratio of UDT to physical drift time (PDT) events at normalization since only PDT events pass the fiducial volume selection. We validate this ratio with an ancillary dataset of events failing S1 and S2 pulse-based selections. When applying the remaining selections, we also confirm that the fraction of UDT events which pass each selection in sequence is consistent between the model and sideband dataset. All comparisons agree to within 1.5σ .

Figure S1 shows the data-model agreement for UDT events restricted to the ROI prior to application of the fiducial volume and the aforementioned S1 and S2 pulse-based selections. The model shows excellent agreement with the data, with a p-value from binned goodness-of-fit tests of 0.28 in $\{S1c, S2c\}$ and 0.38, 0.48 in the S1c, S2c projections, respectively.

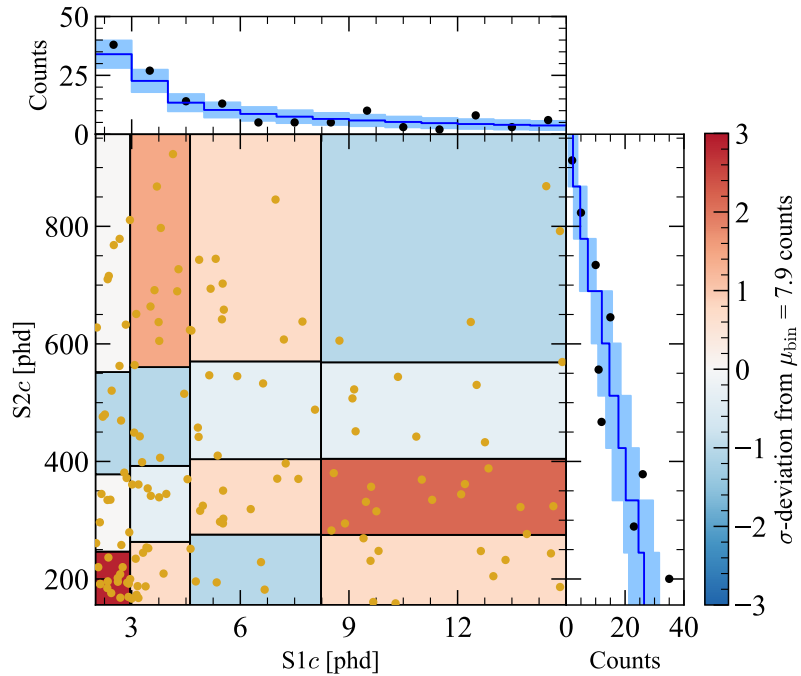


FIG. S1. Data-model agreement for a pure accidental background validation dataset composed of events with unphysical drift time ($\gtrsim 1$ ms), shown in $\{S1c, S2c\}$ and 1D projections. In this comparison, a subset of selection criteria applied to the final dataset is removed for increased statistics. The underlying color plot shows good data-model agreement in units of σ . These bins are defined such that in each the model predicts 7.9 events. The yellow and black dots depict the data, while the blue line and band depict the accidental model prediction and associated Poisson uncertainty.

We test the robustness of this modeling algorithm with ancillary datasets which probe a range of environmental conditions and assumptions. To test the modeling in elevated electron and photon rate environments, we loosen

the hold-off after large energy depositions described in the main text which results in the inclusion of events with approximately 3 and 6 times the mean electron and photon rates in the main science dataset, respectively. We then compare the model to UDT events in this elevated electron and photon rate environment. We also perform the modeling procedure on events during AmLi calibration periods with elevated S1 and S2 pulse rates and check the agreement with UDT events. To test the modeling of PDT events, we compare the data-model agreement for physical drift time events that fail several S1 and S2 pulse cuts. More details on the model construction and validations will be described in a dedicated modeling paper.

Details of the Nuclear Recoil Detector Response Model and Uncertainty Treatment

As described in the main text, the LZ nuclear recoil response model is based on NEST v2.4.5 beta [23] which is tuned to 2.45 MeV DD-neutron-induced xenon nuclear recoils from threshold (1 keV) to the 74 keV endpoint. We employ a Markov Chain Monte Carlo (MCMC) procedure using the EMCEE package [27]. Table S1 shows the default values, priors assumed, and resulting best-fit values for the parameters governing the NR yields, NR fluctuations, and model-specific nuisance parameters. NEST parameters excluded from the table, such as those describing field dependence (e.g. δ), are held fixed at their default values due to a lack of sensitivity.

The yield parameters α , β , γ , and ϵ , as well as the fluctuation parameters F_i and the NR recombination variance coefficient, λ , are given wide flat priors that encompass the NEST default values. F_{ex} is modified in the model to have a linear dependence on the number of excitons N_{ex} , with the functional form $F_{\text{ex}} = aN_{\text{ex}} + b$, with coefficients a and b floated in the fit. The modification of F_{ex} from the NEST default is found to be necessary for good data-model agreement. The parameters controlling the low energy roll-off behavior, ζ , η , θ , ι , have Gaussian prior distributions in the MCMC, with the μ and σ values set by the NEST default mean values and uncertainties, respectively. This choice is motivated by the minimum energy at which this calibration is sensitive (~ 2.5 keV), determined by incrementally increasing the minimum recoil energy included in the model until the fit $\Delta\chi^2$ exceeds 1. These NEST model priors are driven by yields measurements performed down to sub-keV NR energies [25, 26, 28].

We further consider nuisance parameters specific to the physics of the neutron interactions. First, the 2.45 MeV DD neutrons may have their energy degraded in two independent processes due to a) interactions within the DD generator before exiting and b) interactions in intervening detector material before entering the active xenon volume. The DD neutron kinetic energy spectrum used in this analysis is based on dedicated simulations and measurements performed at Brown University prior to deploying the DD generator underground at SURF [54]. These effects manifest in the fraction of <2 MeV neutrons considered in the energy spectrum entering the TPC. Second, we consider uncertainties in the xenon differential elastic-scattering cross-sections by treating JENDL-4.0u [55] and ENDF/B-VII.1 [56] as limiting cases for the single-scatter NR spectrum. Both of these parameters primarily affect the observed recoil spectra at intermediate recoil energies (approximately from 25–50 keV), and are found to be largely uncorrelated with the mean yields and fluctuation parameters.

We study two background populations: accidental coincidences like those described in the text and unresolved multiple scatters - multiple scatter events where the S2s cannot be resolved in time and appear as single scatters. The accidental population is estimated using both UDT events and events where the S1 does not coincide with the DD generator pulse. It is found to have a small predicted rate and limited impact on the best fit yields and fluctuations; thus it is fixed in the fits. The fraction of unresolved multiple scatters is estimated to be approximately 5%-7% using dedicated simulations and a data-driven approach to predict what fraction of the time multiple scatters merge based on the distribution of S2 time separations. This fraction is included in the fitting routine with a flat prior ranging up to 20%.

The systematic uncertainties on L_y , Q_y , and fluctuations in the detector response model are propagated into the statistical inference as discussed in the text. The yield uncertainties are quantified by sampling the MCMC posterior distribution to produce L_y and Q_y curves as a function of energy. These yield curves are then eigen-decomposed, and the two leading order eigenvalues and eigenvectors are mapped back onto corresponding NEST parameters to produce the $\pm 1\sigma$ uncertainty on the best-fit NR yields. The range of yields tested is shown in Fig. S2 and the eigen-decomposition enables us to model both correlated and anti-correlated behavior between L_y and Q_y at threshold. For the fluctuation parameters, only the effect of F_{ex} is considered in the final uncertainty calculation. Uncertainties associated with F_i and recombination fluctuations were determined to have a subdominant impact on the predicted NR signal rate in the ROI. These considerations allow us to reduce the NR response uncertainties on the predicted number of ${}^8\text{B}$ CE ν NS by approximately 30% relative to the default NEST v2.4.0 model [57].

We calculate a combined rate effect of the various systematic uncertainties due to NR modeling and the signal detection efficiencies, parameterized by a single nuisance parameter. This reduces the number of fitted parameters in

the statistical inference procedure described in the main text, which would otherwise introduce degeneracies in the fits. We sample from unit Gaussian distributions for each uncertainty and evaluate the product of the corresponding changes in rate to build a combined effective uncertainty. The assumption that the combined rate change can be constructed as a product of the individual rate changes was explicitly confirmed. This procedure is repeated for each NR component – ${}^8\text{B}$ CE ν NS, DM, and neutrons. We find that incorporating shape effects due to model uncertainties has a negligible impact on the predicted {S1c, S2c} spectra at the level of predicted statistics in the ROI. We also ignore correlations between individual uncertainties, which is a conservative treatment as including correlations would slightly reduce the overall rate uncertainty. The nuisance parameter, σ_{eff} , is included in the statistical inference which controls the relative rate uncertainty for each NR component.

TABLE S1. Default and best-fit model parameters for the NEST NR mean yield (top), NEST NR fluctuations response model (middle), and model nuisance parameters (bottom). See Eq. 6 of Ref. [24] for original definition of yield and fluctuation parameters. In the column labeled *LZ Prior*, the values in the square brackets define upper and lower boundaries of the range in which a parameter may freely float. The values in the curly brackets define the mean and standard deviation of the gaussian providing a constraint within the fit.

NR Yield Parameter	NEST Default	LZ Prior	LZ Posterior
α	$11.0_{-0.5}^{+2.0}$	[8.0, 17.0]	11.6 ± 1.1
β	1.1 ± 0.05	[0.80, 1.25]	$1.084_{-0.021}^{+0.024}$
γ	$(4.80 \pm 0.21) \times 10^{-2}$	[0.015, 0.065]	$(5.29_{-0.06}^{+0.05}) \times 10^{-2}$
ϵ [keV]	$12.6_{-2.9}^{+3.4}$	[2.0, 30.0]	$8.0_{-1.7}^{+1.8}$
ζ [keV]	$(3.0 \pm 1.0) \times 10^{-1}$	{0.3, 0.1}	$(4.4 \pm 1.5) \times 10^{-1}$
η	2 ± 1	{2.0, 1.0}	$1.1_{-0.3}^{+0.5}$
θ [keV]	$(3.0 \pm 0.5) \times 10^{-1}$	{0.3, 0.05}	$(3.0_{-0.9}^{+0.8}) \times 10^{-1}$
ι	2 ± 0.5	{2.0, 0.5}	$2.2_{-0.7}^{+0.8}$

NR Fluctuations Parameter	NEST Default	LZ Prior	LZ Posterior
F_i (constant)	0.4	[0.001, 2.000]	$1.1_{-0.4}^{+0.3}$
F_{ex} (constant)	0.4	[0.001, 8.000]	$1.1_{-0.7}^{+1.4}$
F_{ex} (linear slope)	-	[0.0, 0.1]	$(2.2 \pm 0.6) \times 10^{-2}$
λ (recombination variance)	1	[0.01, 1.2]	$(2.9_{-1.7}^{+2.2}) \times 10^{-1}$

Nuisance Parameter	LZ Prior	LZ Posterior
< 2 MeV neutron fraction	[0.0, 0.3]	$(1.3 \pm 0.3) \times 10^{-1}$
JENDL/(ENDF+JENDL) Fraction	[0.0, 1.0]	$(7.0_{-1.4}^{+1.3}) \times 10^{-1}$
Unresolved multi-scatter background fraction	[0.0, 0.2]	$(5.0_{-1.0}^{+1.1}) \times 10^{-2}$
Accidental coincidence background fraction in low energy region	0.037	-

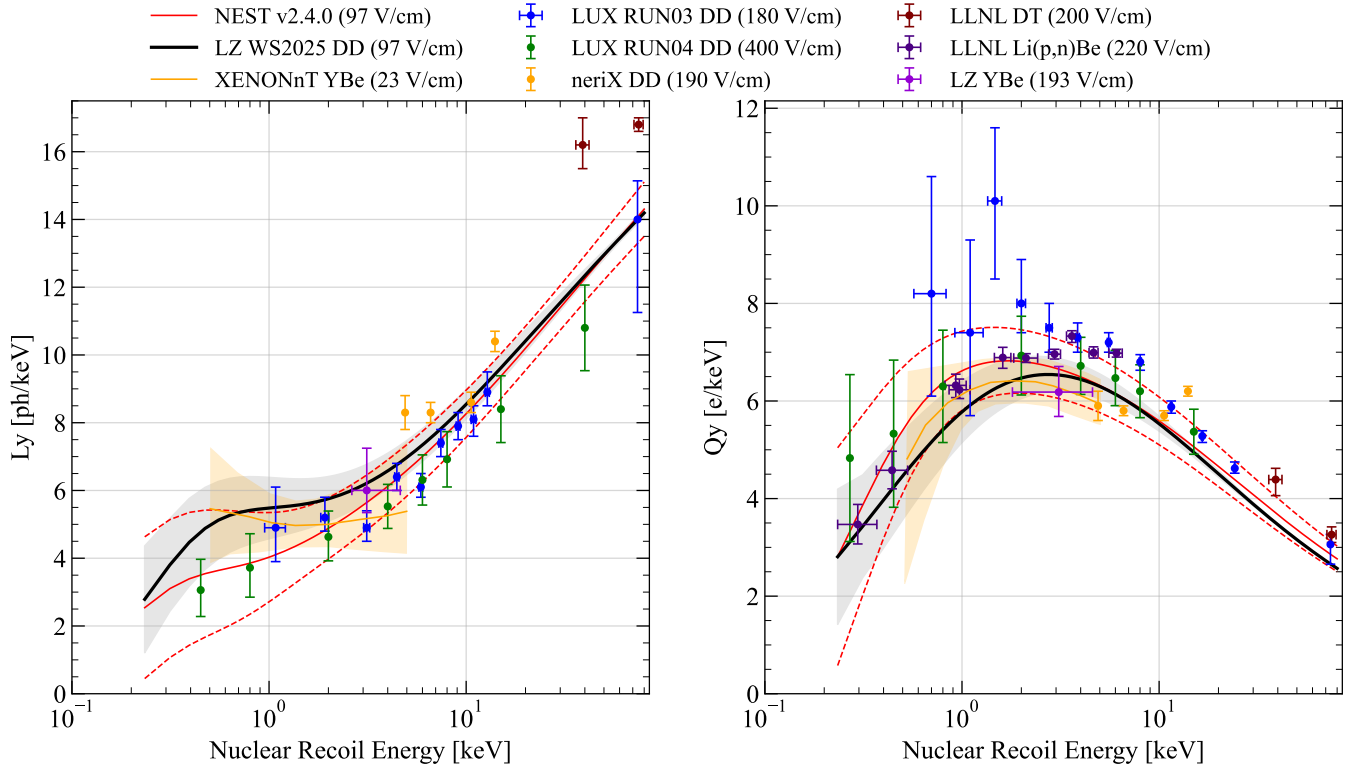


FIG. S2. The mean light yield, L_y , and charge yield, Q_y , used in this analysis are shown as black lines. The $\pm 1\sigma$ uncertainty is shown as shaded gray envelope which considers the yield uncertainties from the calibration procedure discussed in the text. The mean and $\pm 1\sigma$ Q_y and L_y curves from the predicted NEST v2.4.0 NR response model at 97 V/cm is shown in red [57]. Yield measurements from LZ [58] and other experimental results are also shown [25, 26, 28, 59–62].

Details on Bias Mitigation

As described in main text, artificial ${}^8\text{B}$ CE ν NS-like and DM-like signal events were randomly injected into the data pipeline. The rate and distribution of the DM-like signal events are discussed in detail in the text and supplements of [3]. The artificial ${}^8\text{B}$ CE ν NS events are constructed in the same manner as the artificial DM-like signal events, but have a distribution following the predicted ${}^8\text{B}$ CE ν NS recoil spectrum.

The injected yearly rate of the ${}^8\text{B}$ CE ν NS artificial events is drawn from a Poisson distribution of mean 4 events and was randomly introduced into the dataset covering 59% of the data collection period. We chose the rate to match the Poisson uncertainty on the single scatter rate of ${}^8\text{B}$ CE ν NS in the fiducial liquid xenon volume using the NR response model and fiducial volume definition of [3]. After considering detection efficiencies and live time losses, the expected number of artificial events from both high mass DM and ${}^8\text{B}$ CE ν NS in our dataset follows a Poisson distribution with a mean of 1.75 events. The number of events injected into the raw data is allowed to be any number (including zero) drawn from this distribution. The true number of injected events is still hidden to the collaboration so as to not impact the bias mitigation of ongoing and future analyses. Only the identity of the 1 event passing the ROI and fiducial volume selection of this analysis was revealed. This event passed all of the data selection criteria described in the main text.

Limits in Terms of Number of DM Events

Figure S3 shows the the WS2025 upper limits in terms of number of DM events.

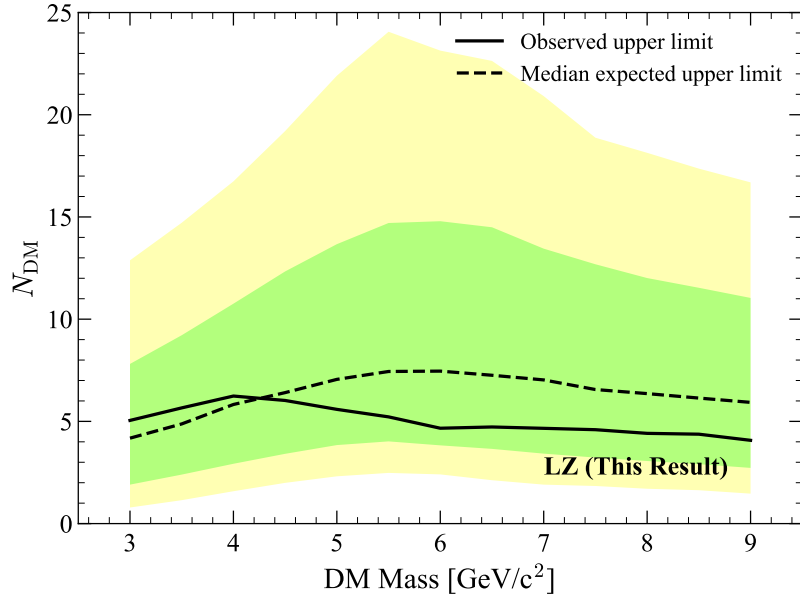


FIG. S3. Upper limits (90% confidence level) on the number of DM events as a function of its mass are shown as a solid black line, for the spin-independent case. Green and yellow regions show the range of expected upper limits from 68% and 95% of the background-only experiments, respectively. The dashed black line shows the median expected upper limit using the post-fit model.